INORGANIC CHEMISTRY FRONTIERS

RESEARCH ARTICLE

View Article Online
View Journal | View Issue



Cite this: *Inorg. Chem. Front.*, 2024, **11**, 7098

# High performance NIR-I to NIR-II emission of a $Cr^{3+}$-doped $Cs_2NaLuCl_6$ phosphor with an IQE and EQE of up to 92.9% and 60.75%†

Fengmei Zhu,[a,c] Yuan Gao *[a,b] and Jianbei Qiu *[a,b,c]

Received 6th June 2024,
Accepted 2nd September 2024

DOI: 10.1039/d4qi01418a

rsc.li/frontiers-inorganic

Presently, there is a need to expand the near-infrared (NIR) emission range, especially in the bio-transparent window, to improve the internal quantum efficiency and external quantum efficiency, and to minimize the shortcomings of luminescence properties. In this work, an ultra-broadband NIR emission $Cr^{3+}$-doped $Cs_2NaLuCl_6$ all-inorganic metal halide perovskite phosphor was synthesized by a grinding–sintering method. Under 300 nm excitation, $Cs_2NaLuCl_6$:$Cr^{3+}$ phosphors exhibited ultra-broadband NIR emission of 800–1400 nm, which covers nearly the entire NIR-I (700–1000 nm) and NIR-II (1000–1400 nm) regions; the emission peaked at around 960 nm, with a full width at half maximum of ~182 nm. Noticeably, the internal- and external-quantum efficiencies of the optimized $Cs_2NaLuCl_6$:$Cr^{3+}$ phosphor were as high as ~92.9% and ~60.75%, respectively. We showed through analysis and simulation that the weak crystal field strength is conducive to increasing the odd term of the crystal field, and therefore it partially released the restriction imposed by the parity prohibition law and improved the energy absorption efficiency of $Cr^{3+}$. As the size of the phosphor approaches the wavelength of NIR luminescence, the apparent Mie scattering effect starts to take effect, which enhances the light extraction of NIR luminescence in the radial direction.



## 1. Introduction

Near-infrared (NIR) luminescence technology has many applications in the fields of optical anti-counterfeiting, night vision display, telecommunications, solar energy harvesting, *etc*. NIR light has the features of rapid responsiveness, non-destructiveness, biological transparency and high tissue penetration and is particularly useful in agriculture and in biomedical imaging and detection.[1–5] For example, the NIR first region (NIR-I, $\lambda$ = 700–1000 nm), such as a $\lambda$ = 730 nm NIR light source, is used for indoor plant lighting because it can react with phytochromes; the $\lambda$ = 800–1000 nm range can be used for night vision monitoring and face recognition, while the NIR second region (NIR-II, $\lambda$ = 1000–1500 nm) bandwidth is more suitable for high-resolution optical bioimaging and chemical analysis due to its low auto-fluorescence, high signal-to-noise ratio and deep tissue penetration.[6–9] Currently, commercial NIR light sources mainly include tungsten incandescent lamps, NIR LEDs, and NIR lasers. Among them, tungsten filament incandescent lamps provide ultra-broad continuous light from visible to NIR light, but they suffer from low energy efficiency, especially the NIR light fraction, high operating temperature, a short service life, and bulky sizes.[10] Newer generation NIR LED and laser sources are compact and more energy efficient. They produce less heat and deliver NIR with higher luminous intensity, though the relative narrow emission wavelength with a full width at half-maximum (FWHM) of up to 40 nm restricts their use for broad spectroscopic analysis.[11,12] Therefore, a new NIR phosphor with efficient broadband NIR emission capacity is highly desirable. By combining NIR phosphors with commercial high-efficiency (ultraviolet) UV/blue LED chips, a new type of phosphor-converted near-infrared light-emitting diode (NIR pc-LED) light source can be built, which has the advantages of low cost, good stability, high power, energy saving and environmental protection.[13–17] Among them, the $Cr^{3+}$ ion is a well-known NIR luminescence center, whose $3d^3$ electronic configuration and optical properties can be readily influenced by the crystal field environment and electron–phonon coupling; therefore, $Cr^{3+}$-doped host materials often demonstrate a broad and tunable range for NIR emission.[18,19]

Recently, all-inorganic metal halide perovskite matrices have attracted much attention for the research and develop-

[a]*Faculty of Material Science and Engineering, Kunming University of Science and Technology, Kunming 650093, China. E-mail: 1251719335@qq.com, qiu@kust.edu.cn*
[b]*Key Laboratory of Advanced Materials of Yunnan Province, Kunming 650093, China*
[c]*Southwest United Graduate School, Kunming 650092, China*

† Electronic supplementary information (ESI) available. See DOI: https://doi.org/10.1039/d4qi01418a

ment of photo-optical materials due to their high light absorption coefficient, excellent carrier mobility, high tolerability towards structural defects and high quantum efficiency. The twin perovskite structure has a general chemical formula such as $A_2B^IB^{III}X_6$ (A = $Cs^+$; $B^I$ = $Cu^+$, $Ag^+$, $Na^+$; $B^{III}$ = $Ln^{3+}$, $Bi^{3+}$, $In^{3+}$; X = $Cl^-$, $Br^-$, $I^-$), A, B and X occupy fixed positions. There are 6 halogen atoms surrounding each B atom in a regular octahedron [$BX_6$] form. $Cr^{3+}$ preferentially enters the center of the octahedron, and its broadband NIR luminescence properties can be adjusted according to the strength of the crystal field.[20–22] So far, the reported NIR phosphors with $Cr^{3+}$ in the octahedron as the luminescence center have suffered from having a low external quantum efficiency (EQE) value, despite having a substantially high internal quantum efficiency (IQE) value, as indicated in Fig. 1a, which lists both IQE and EQE test values of a panel of $Cr^{3+}$-doped NIR luminescent materials. EQE, but not IQE, ultimately determines the performance of a lighting device.[23–90] Few have reported a $Cr^{3+}$-doped NIR luminescent material that covers the NIR-I and NIR-II regions with high IQE and EQE values.

Here we report the synthesis of $Cr^{3+}$-doped $Cs_2NaLuCl_6$ NIR phosphors with an all-inorganic metal halide double perovskite structure by a grinding and sintering method. Excited by UV light (@ 300 nm), this phosphor effectively emitted 800–1400 nm ultra-broadband NIR covering the NIR-I to NIR-II regions. The emission peak was located at 960 nm and had a half-peak width of ~182 nm. The IQE and EQE were 92.9% and 60.75%, respectively. We showed that the unique broadband emission originated from the $^4T_2(F) \rightarrow {}^4A_2(F)$ allowed transition of $Cr^{3+}$ in the octahedra of the double perovskite structure. The structure–optical property relationship between the NIR luminescence centers and the host materials led to a high IQE and EQE, and the principles behind the ultra-broadband emission covering the NIR-I to NIR-II regions were explored. We also demonstrated the potential applications of NIR pc-LED light sources for the purpose of night vision imaging acquisition.

# 2. Experimental

## 2.1 Materials

CsCl (99.99%), NaCl (99.99%), $LuCl_3{\cdot}6H_2O$ (99.99%), and $CrCl_3{\cdot}6H_2O$ (99.99%) were purchased from Aladdin Chemical Reagent Co., Ltd. All chemicals were used as received without any further purification.

## 2.2 Synthesis of the $Cs_2NaLuCl_6$:$xCr^{3+}$ phosphor

CsCl (2 mmol), NaCl (1 mmol), $LuCl_3{\cdot}6H_2O$ (1 − $x$ mmol), and $CrCl_3{\cdot}6H_2O$ ($x$ mmol) ($x$ = 0, 0.005, 0.008, 0.01, 0.012, and 0.017) were thoroughly mixed by grinding in an agate mortar with a small amount of deionized water as the wetting agent for 30 minutes until a uniform powder was obtained. It was transferred to an alumina crucible, covered with a lid, sintered in air at 623 K for 2 hours, then slowly cooled to room temperature, and finally ground to powder before use. These samples were referred to as CNLC:$x$Cr ($x$ = 0, 0.005, 0.008, 0.01, 0.013, 0.015, and 0.017).

## 2.3 Characterization

The phases of the samples were examined by X-ray diffraction (XRD) measurements on a Bruker AXS ADVANCE diffractometer using Cu Kα radiation ($\lambda$ = 1.5406 Å) at 40 kV and 40 mA. The diffraction data were collected in the range of 10°–80° with a step size of 0.01 ($2\theta$) at a step time of 0.2 s. Rietveld refinement was employed using Fullprof software. X-ray photoelectron spectra (XPS) were recorded on an ESCALAB 250 photoelectron spectrometer (Thermo Fisher Scientific, USA) with Al Kα (1486.6 eV) as the X-ray source. The morphological characteristics were evaluated using a scanning electron microscope (SEM, SU8000, Hitachi) equipped with an energy dispersive X-ray spectroscopy (EDS) system. Photoluminescence (PL) and excitation photoluminescence (PLE) spectra were recorded on a spectrofluorometer (Horiba 8000, Horiba) equipped with a 75 W Xe lamp as excitation, and an InGaAs DDS detector was connected. Diffuse reflection (DR) spectra were recorded by a UV-Vis-NIR spectrophotometer (U-4100, Hitachi) with an integration sphere. The electron spin resonance (EPR) spectra were recorded at 293 K on a Bruker EMX PLUS EPR spectrometer operating in the X-band (about 9.205 GHz) with a field modulation frequency of 100 kHz. The magnetic field was scanned from 260 to 360 mT and the microwave power used was 10 mW. A powdered phosphor of 20 mg was taken in a quartz tube for EPR measurements. The NIR internal quantum yield (IQE), absorption efficiency value, and NIR luminescence decay time were measured using an integrated sphere on the Edinburgh FLS1000 spectrophotometer. The temperature-dependent PL spectra were collected by a measurement system containing a heating stage, which gives time-integrated intensities. Electroluminescence (EL) spectra and the performances of the fabricated NIR pc-LED devices were measured using an integrating sphere (Labsphere), and data were collected using a multichannel photodetector (MCPD-9800, Otsuka Photal Electronics). Visible images and NIR images were obtained using a visible camera (Canon EOS6D Mark II, respond wavelength: 300–700 nm) and an NIR camera (VIR APR1, respond wavelength: 400–1100 nm), respectively.

## 2.4 Computational model

The CASTEP package of Material Studio was used to simulate the electron density of a $Cs_2NaLuCl_6$ lattice based on parameters of the crystal structure obtained from Rietveld refinement analysis. A generalized gradient approximation with the Perdew–Burke–Ernzerhof functional was adopted. We defined the convergence criteria for the energy task as ultra-fine quality, including a custom energy cutoff of 660.00 eV, SCF tolerance of $5 \times 10^{-7}$ eV per atom, and $K$-point of 4 × 4 × 4. These computational parameters were derived by optimization based on trial and error. The forward-direction scattering by the single micro-particle was simulated using the finite element method (COMSOL). The outer frame of the simulation model consists of a sphere (diameter = 30 μm) surrounded by a per-

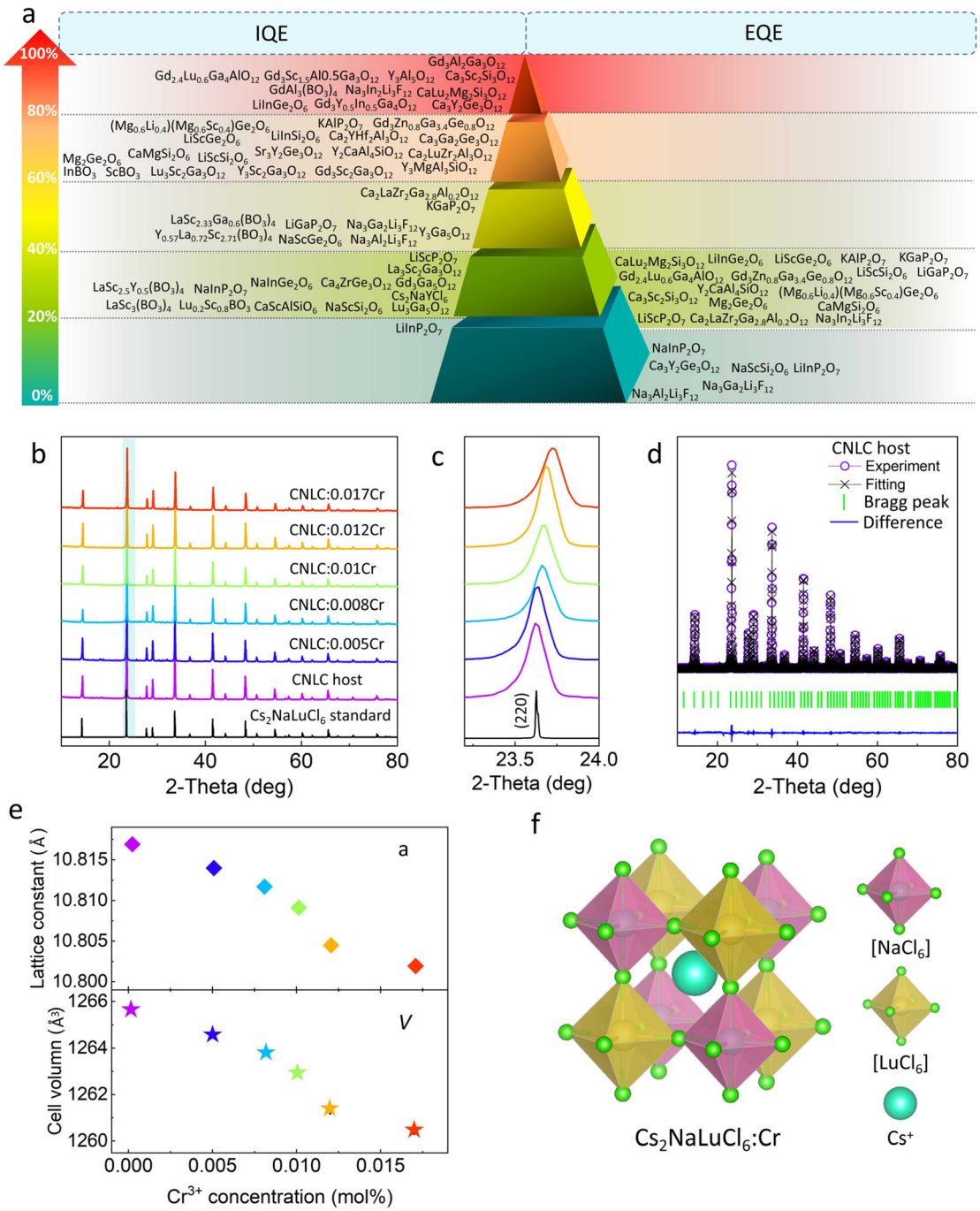


**Fig. 1** (a) Survey of reported $Cr^{3+}$-doped NIR phosphors. Taking the IQE/EQE value as the *Y*-axis, the value of IQE on the left side and the value of EQE on the right side are summarized. (b) Measured XRD pattern and (c) the magnified XRD patterns in the angle range of 23.2–24° of CNLC:*x*Cr (*x* = 0, 0.005, 0.008, 0.01, 0.012, and 0.017), respectively. (d) The Rietveld refinement of the $Cs_2NaLuCl_6$ host. (e) Variation of lattice parameters *a* and *V* of CNLC:*x*Cr (*x* = 0, 0.005, 0.008, 0.01, 0.012, and 0.017), respectively. (f) Schematic diagram of the crystal structure of $Cs_2NaYCl_6$.

fectly matched layer (PML) (thickness = 3 μm). The sphere model was divided into two parts: all part composed of air ($n$ = 1.00), and single micro-particle (diameter = 1.5 μm, $n$ = 1.75) in the *xy*-plane was located on the central point of the sphere. The incident light ($\lambda$ = 960 nm) from the port was allowed to propagate from the bottom to the upper side at $\theta_{in}$ = 0°. The far-field scattering intensity was integrated along the boundary edge between the PML and air in the *xz*-plane.

### 2.5 Fabrication of a NIR pc-LED device

A NIR pc-LED device was fabricated using the optimized NIR phosphor and a commercial UV LED chip (@ ~300 nm).

 

Typically, the as-prepared CNLC:0.008Cr phosphor was thoroughly mixed with epoxy resin (1 : 1) and coated on the chip; then it was heated at 353 K for 10 h to obtain a NIR pc-LED device.

## 3. Results and discussion

Fig. 1b shows the X-ray diffraction patterns of CNLC:*x*Cr ($x$ = 0, 0.005, 0.008, 0.01, 0.012, and 0.017) with different doping concentrations of $Cr^{3+}$ ions. The diffraction peaks of the measured samples corresponded well with the standard diffraction pattern, indicating that the synthesized CNLC:*x*Cr had relative phase purity and $Cr^{3+}$ doping did not have a significant impact on the phase purity of the matrix.[91,92] In addition, Fig. 1c shows a partially enlarged XRD diffraction peak of CNLC:*x*Cr in 23.2–24° corresponding to the (220) crystal plane position. It shows that with the increase of $Cr^{3+}$ doping amount, the diffraction peak gradually shifts to a larger angle, which suggests that ions with smaller ionic radii replaced the larger ones, which caused the lattice to shrink. Considering the ionic radii of $Cs^+$ (CN = 12, $r$ = 1.88 Å), $Na^+$ (CN = 6, $r$ = 1.02 Å), $Lu^{3+}$ (CN = 6, $r$ = 0.86 Å) and $Cr^{3+}$ (CN = 6, $r$ = 0.615 Å) in the CNLC crystal (Å), together with the similarity in valence and Bragg's law, it is most likely that it was $Cr^{3+}$ that replaced $Lu^{3+}$ and occupied the center position in octahedra. To gain a better understanding on the crystal structure of the $Cs_2NaLuCl_6$ phosphor, we carried out Rietveld refinement on the host phosphor with Fullprof software. Fig. 1dshows the refined spectrum of the matrix sample. The refined data showed the $Cs_2NaLuCl_6$ host as a pure phase, and the $R_p$ and $R_{wp}$ values were 5.87% and 5.22%, respectively, and the $\chi^2$ value was 2.64%. The powder diffraction data fitted well with the data listed in the standard card. To further probe into the crystal structure of a CNLC:*x*Cr phosphor and clarify the nature of ion replacement by $Cr^{3+}$, we did Rietveld refinement on the CNLC:*x*Cr phosphor. The fitting results are shown in Fig. S1,† and the crystallographic parameters obtained from the refinement are listed in Table S1.† These results suggest that the CNLC:*x*Cr phosphors belong to the cubic phase in the space group $Fm\bar{3}m$ (225). As shown in Fig. 1e, the unit cell constant ($a$) and unit cell volume ($V$) of the $Cs_2NaLuCl_6$ lattice decreased with the increase of $Cr^{3+}$ doping amount, which is consistent with the notion that $Cr^{3+}$ with smaller ionic radius (CN = 6, $r$ = 0.615 Å) instead of $Lu^{3+}$ (CN = 6, $r$ = 0.86 Å) with larger ionic radius, occupies the center of octahedra in the matrix lattice, causing the apparent shrinkage. Fig. 1f shows the spatial configuration of the crystal structure of $Cs_2NaLuCl_6$, that is each of the $Na^+$ and $Lu^{3+}$ ions bonds with six $Cl^-$ ions to form regular octahedra [$NaCl_6$] and [$LuCl_6$], and these octahedra are connected at the same vertices, along three directions spatially to form a cubic structure; $Cs^+$ ions are located in the gap positions of the octahedra to fill in, forming a three-dimensional double perovskite structure.

Fig. 2a shows schematically the preparation process of $Cs_2NaLuCl_6$:$xCr^{3+}$ phosphors. All chlorides were mixed accord-

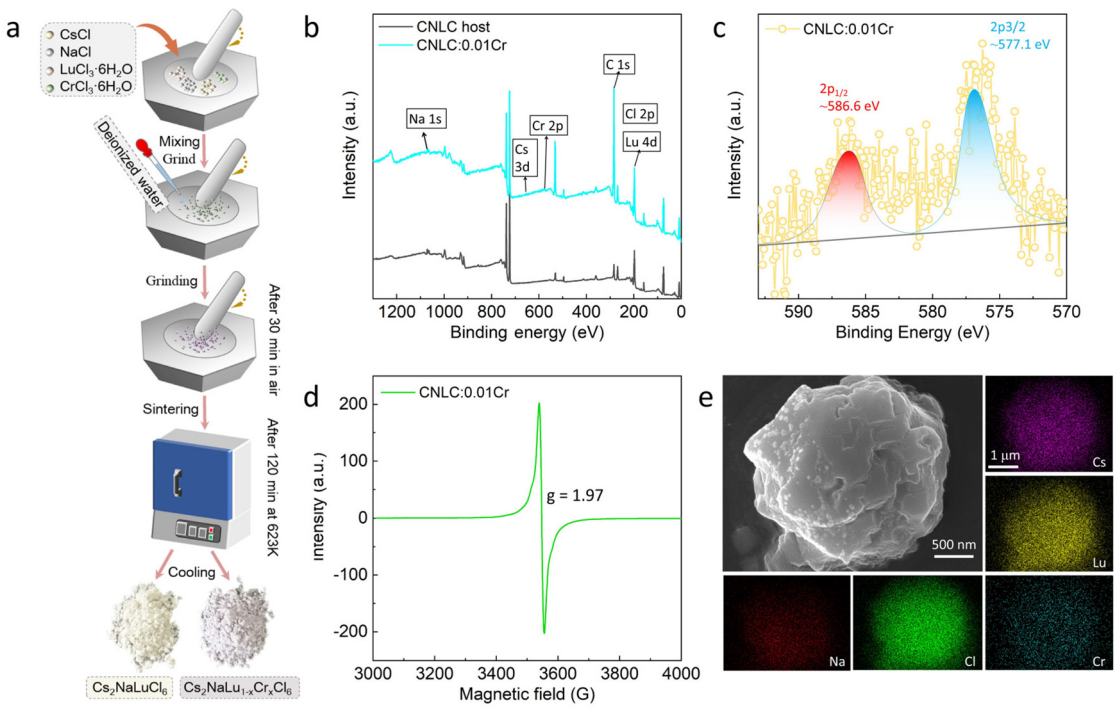


**Fig. 2** (a) Schematic illustration of the synthesis process used for the CNLC:*x*Cr phosphor *via* the grinding–sintering method. (b) Full XPS curves and (c) fine spectra of the CNLC and CNLC:0.01Cr phosphors, respectively. (d) Room temperature EPR spectrum of the CNLC:0.01Cr phosphor. (e) SEM image and element mapping images of the CNLC:0.01Cr sample.

ing to the stoichiometric ratio with the help of the appropriate amount of deionized water by grinding at room temperature and sintering in a muffle furnace at 623 K. Fig. 2b shows the XPS spectra of the $Cs_2NaLuCl_6$ matrix and the CNLC:0.01Cr phosphor. The peaks of Cs, Na, Lu, Cl, and Cr can be identified. Two peaks of XPS fine spectrum at 577.1 and 586.6 eV in Fig. 2c were from $Cr^{3+}$ in $2p_{3/2}$ and $2p_{1/2}$ states, which indicates that the valence state of Cr in CNLC:0.01Cr is +3.[93,94] ESR is an appropriate method to reflect the valence state and the occupation status of paramagnetic transition metal ions. Fig. 2d shows the ESR spectrum of the CNLC:0.01Cr phosphor at room temperature, and an obvious resonance signal is present ($g$ = 1.97), which is mainly caused by the $Cr^{3+}$–$Cr^{3+}$ coupled exchange as ion pairs; and the results reflect the fact that Cr ions finally entered the $Cs_2NaLuCl_6$ matrix lattice in the +3 state.[95] The morphology, particle size and size distribution are known to have a significant impact on the luminous efficiency of phosphor powder and can influence the outcome of the encapsulation process during LED casting. The SEM picture showed that CNLC:0.01Cr powder consisted of relatively smooth spherical particles of 1.5–2 μm in size, which are agglomerated by smaller nano-sized particles of 50–70 nm. The submicron size is susceptible to Mie scattering of NIR luminescence, which could improve the external quantum efficiency of NIR emission (Fig. 2e).[96–99] The SEM-EDS mapping showed that Cs, Na, Lu, Cr and Cl elements were evenly distributed on the surface of the particles. The ESD spectrum of CNLC:0.008Cr showed that the atomic ratio is Cs : Na : Lu : Cl : Cr = 2 : 1 : 0.932 : 0.0075 : 6, which is consistent with the chemical formula within the error range (Fig. S2†).

Fig. 3a shows the diffuse reflectance spectra of CNLC:0.008Cr ($x$ = 0, 0.005, 0.008, 0.01, 0.012, and 0.017)

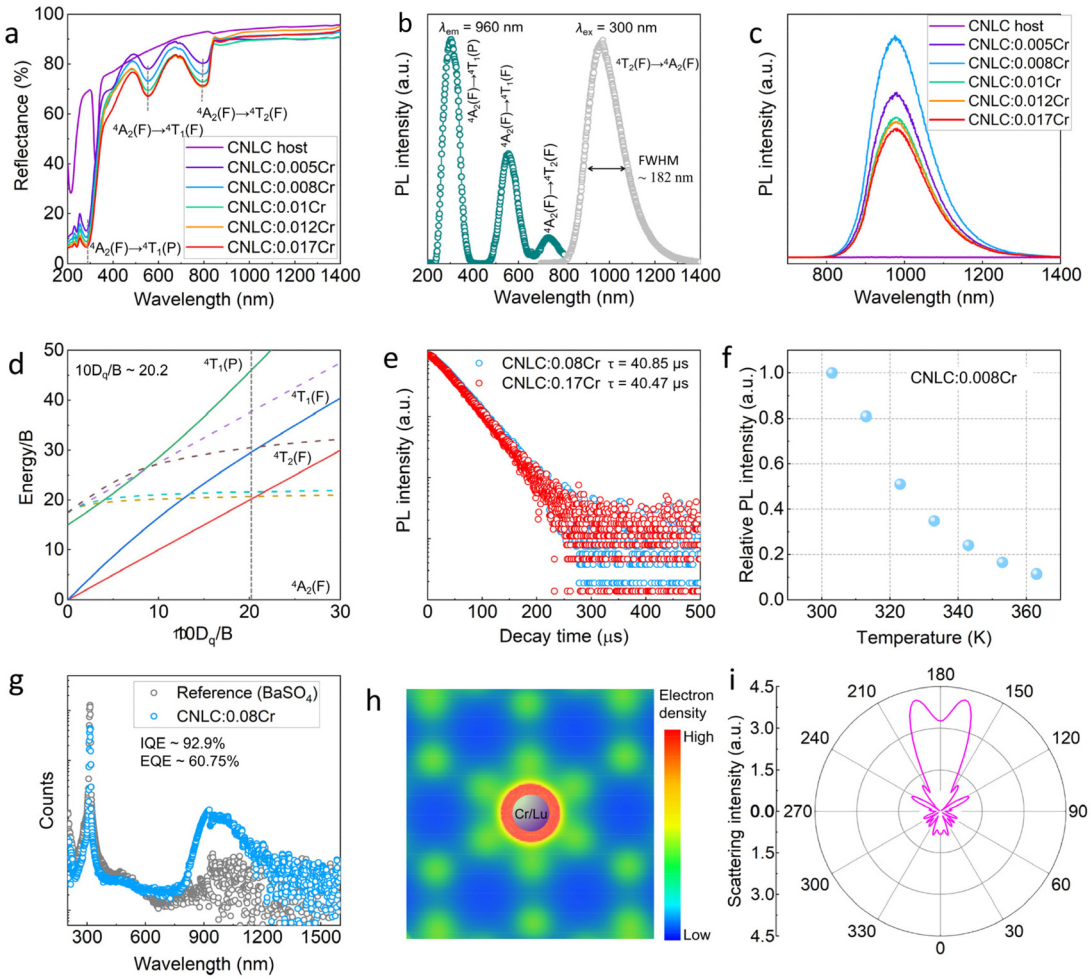


**Fig. 3** (a) Diffuse reflectance spectra of the as-prepared CNLC:$x$Cr phosphor. (b) Photoluminescence excitation and emission spectra of the CNLC:Cr phosphor. (c) Measured NIR spectra of the CNLC:$x$Cr phosphor excited at 300 nm, $x$ = 0, 0.005, 0.008, 0.01, 0.012, and 0.017, respectively. (d) Tanabe–Sugano energy level diagram for $Cr^{3+}$ ions in the octahedral crystal field of $Cs_2NaLuCl_6$ compounds. (e) NIR luminescence decay curves of the CNLC:0.008Cr and CNLC:0.017Cr phosphors ($\lambda_{ex}$ = 300 nm and $\lambda_{em}$ = 960 nm), respectively. (f) Relative integral intensity of temperature-dependent emission spectra of the CNLC:0.008Cr phosphor. (g) Measured NIR PLQY of the reference and the MTO:0.06Ni sample, respectively. (h) Simulated electron density of $Cr^{3+}$-doped CNLC system. (i) COMSOL Multiphysics software simulation of the far-field radiation distribution of a single micro-particle at $\lambda_{em}$ = 960 nm light.

 

phosphors. Three obvious absorption bands were present from the ultraviolet to near-infrared range, located in the 250–350 nm, 530–670 nm, and 700–900 nm ranges, respectively. These absorption peaks correspond to $^4A_2(F) \rightarrow {}^4T_1(P)$, $^4A_2(F) \rightarrow {}^4T_1(F)$, and $^4A_2(F) \rightarrow {}^4T_2(F)$ electronic transitions of $Cr^{3+}$ ions, respectively. Based on the method of Tauc plot,[100] we used the data of diffuse reflectance of the $Cs_2NaLuCl_6$ matrix and derived that the band gap of the matrix is 5.37 eV (Fig. S3†), and no additional defect level absorption was observed in the matrix, indicating that $Cs_2NaLuCl_6$ is a suitable matrix material for NIR phosphor. Fig. 3b shows the excitation and emission spectra of CNLC:0.008Cr phosphor at room temperature. Two obvious excitation peaks located at 300 nm and 555 nm were present in the excitation spectrum, which correspond to the electronic transitions of $^4A_2(F) \rightarrow {}^4T_1(P)$ and $^4A_2(F) \rightarrow {}^4T_1(F)$ of $Cr^{3+}$ ions, respectively. These data were consistent with the diffuse reflectance spectrum. Under ~300 nm UV light excitation, the emission spectrum exhibited an ultra-broadband emission peak (700–1400 nm) that covers the NIR-I to NIR-II region, with a FWHM of 182 nm, which corresponds to the $Cr^{3+}$:$^4T_2(F) \rightarrow {}^4A_2(F)$ spin allowed transition. Fig. 3c shows the emission spectrum of the CNLC:$x$Cr ($x$ = 0, 0.005, 0.008, 0.01, 0.012, and 0.017) phosphors under 300 nm excitation. As the doping contents of $Cr^{3+}$ ions gradually increased, the emission intensity of NIR first increased, peaked at 0.8 mol%, and then decreased due to a concentration-dependent quenching effect. The optical properties of $Cr^{3+}$ are very sensitive to the strength of the crystal field, and the parameters of the peak position and peak width of an emission peak are also closely related to the strength of the crystal field. According to the theory of crystal field, the Tanabe–Sugano energy level diagram is valuable to analyze the energy level distribution of electron configuration. The energy level distribution of $Cr^{3+}$ in the $3d^3$ configuration is shown in Fig. 3d, which can be described by the Tanabe–Sugano schematic diagram as:[101–106]

$$10D_q = E(^4T_2) \quad (1)$$

$$\frac{D_q}{B} = \frac{15(x-8)}{x^2-10x} \quad (2)$$

$$x = \frac{E(^4T_1) - E(^4T_2)}{D_q} \quad (3)$$

where $B$ is the Racah electron repulsion parameter, $D_q$ is the crystal field parameter, $E(^4T_2)$ and $E(^4T_1)$ were determined by the energy positions of the excitation peaks $^4A_2 \rightarrow {}^4T_2$ and $^4A_2 \rightarrow {}^4T_1$ energy levels, respectively. The calculated $10D_q/B$ value of CNLC:$x$Cr phosphors was 20.2, which indicates that the $Cs_2NaLuCl_6$ matrix provides a weak crystal field environment for $Cr^{3+}$. To further explain the mechanisms of phosphor luminescence and energy transfer, the NIR luminescence decay time at 960 nm, under 300 nm excitation of CNLC:0.008Cr and CNLC:0.017Cr phosphors, was separately monitored; as shown in Fig. 3e, the average fluorescence lifetimes were 40.85 and 40.47 μs, which are close to the reported NIR luminescence lifetimes of $^4T_2(F) \rightarrow {}^4A_2(F)$ spin allowed transitions from $Cr^{3+}$ located in the octahedra. In addition, the lifetimes of CNLC:$x$Cr phosphors fit very well to the pattern of the mono-exponential decay curve, which shows that the energy transfer between $Cr^{3+}$ ions is negligible, which could contribute to a higher luminescence internal quantum efficiency.[107,108] Thermal stability is an important factor affecting the performance of luminescent materials, especially for phosphor materials used in NIR pc-LED devices expected to be exposed to high temperature under high output power. Generally, the reason for the temperature-dependent decrease in luminous intensity is that when the temperature rises, the lattice vibration intensifies, so is the lattice relaxation of the luminescence center, which increases the probability of no radiation transition, and thus a decrease in luminous efficiency. Fig. 3f shows the temperature–wavelength emission spectrum of the prepared CNLC:0.008Cr phosphor from room temperature (@ 293 K) to 373 K under the excitation of 300 nm ultraviolet light. As the temperature was raised, the peak shape and peak position of the emission spectra remained basically unchanged, and the luminous intensity decreased due to thermal quenching caused by an increased probability of a non-radiative transition at high temperature. To further study the thermal quenching process, the thermal activation energy ($E_a$) of the CNLC:0.008Cr phosphor was evaluated using the Arrhenius formula. As shown in Fig. S4.† The value of $E_a$ was calculated to be 0.175 eV by plotting the function of $\ln[(I_0/I_T) - 1]$ and $1/K_BT$.[109,110] The luminescence quantum efficiency of the phosphor is crucial to the performance of NIR pc-LED light source devices. As shown in Fig. 3g, the NIR IQE value of the CNLC:0.008Cr phosphor that showed the highest NIR emission intensity is 92.9%, and the absorption rate of the phosphor is 0.6, so its NIR EQE value is as high as 60%, which is much higher than the known $Cr^{3+}$- doped NIR phosphor materials. Next, we analyzed the possible mechanisms that led to the high IQE and EQE values of the CNLC:0.008Cr phosphor. The charge density of octahedra and the unit cell symmetry were simulated with the Material Studio software. The distribution of charge density of a CNLC:0.008Cr unit cell around the center of the $[Y/CrCl_6]$ octahedron is shown in Fig. 3h. It shows a high charge density, but the distribution of charge density in the center of the octahedron is highly symmetric. Also, we evaluated the degree of distortion of the octahedra before and after $Cr^{3+}$ doping based on the refined XRD results and found that the distortion of the $CrCl_6$ octahedra was negligible. The results support the conclusion derived from the visual simulation that the octahedra are highly symmetric. For this reason, the $Cr^{3+}$ ions are weakly influenced by the crystal field strength. This results in a broadband NIR emission with a large Stokes shift, which is consistent with the results of the Tanabe–Sugano theoretical calculation. It is important to point out that a weak strength of crystal field is beneficial for increasing the odd term of the crystal field, thereby partially releasing the restriction by the parity prohibition law, improving the efficiency of energy absorption by $Cr^{3+}$ ions in $Cs_2NaLuCl_6$ crystals, and contributing to the high IQE

and absorptivity, thus a high EQE value of CNLC:0.008Cr.[111,112] On the other hand, we used COMSOL Multiphysics software to simulate the far-field scattering effect on NIR fluorescence of CNLC:*x*Cr phosphor (Fig. 3i). The apparent Mie scattering effect occurs when particles of 1 μm in diameter meet with NIR emission (the wavelength is about 0.98 μm); the NIR light is strongly scattered radially, which greatly reduces the loss of NIR light and boosts both the IQE and EQE.[113,114]

We fabricated a NIR pc-LED device with a commercial 300 nm UV LED chip and CNLC:0.008Cr phosphors. To ensure a high performance, a heat-dissipating aluminum sheet was welded on the back of the UV chip. The CNLC:0.008Cr phosphor was mixed with silica gel at a weight ratio of 1 : 1 and applied on the surface of the semiconductor chip and cured to complete the packaging.[115–126] Fig. 4a shows the electroluminescence (EL) spectrum of the packaged NIR pc-LED driven under 60 mA direct current (voltage @ 3 V). It showed a narrow band of the UV LED at 300 nm and a broadband NIR emission of the phosphor at 800–1400 nm. Given the unique nature of shortwave NIR, we proposed a range of applications for the NIR pc-LED. Under the illumination of a white LED, the luminescence of the NIR pc-LED device underneath a long-wavelength filter could not be displayed with an ordinary digital camera (Fig. 4b, left); however, the NIR luminescence underneath the same long-wavelength pass filter was clearly captured with a NIR camera, because visible light was not blocked by this filter, highlighting a potential NIR anti-counterfeiting application. The images in Fig. 4c and d are the pictures under natural light taken with an ordinary camera and with a NIR camera, respectively. Fig. 4e shows the picture taken with a NIR camera using NIR produced by NI-LED as the light source. The objects are metal screws (left side of Fig. 4c), color patterns (left side of Fig. 4d) and a logo (upper side of Fig. 4e), respectively. The corresponding imaging captured by the NIR camera clearly revealed the outlines of these objects, indicating that the NIR light source emitted from a NIR pc-LED (1 W) prepared from a 300 nm UV chip and the CNLC:0.008Cr phosphor performed well for night vision imaging under a very weak luminescent condition.

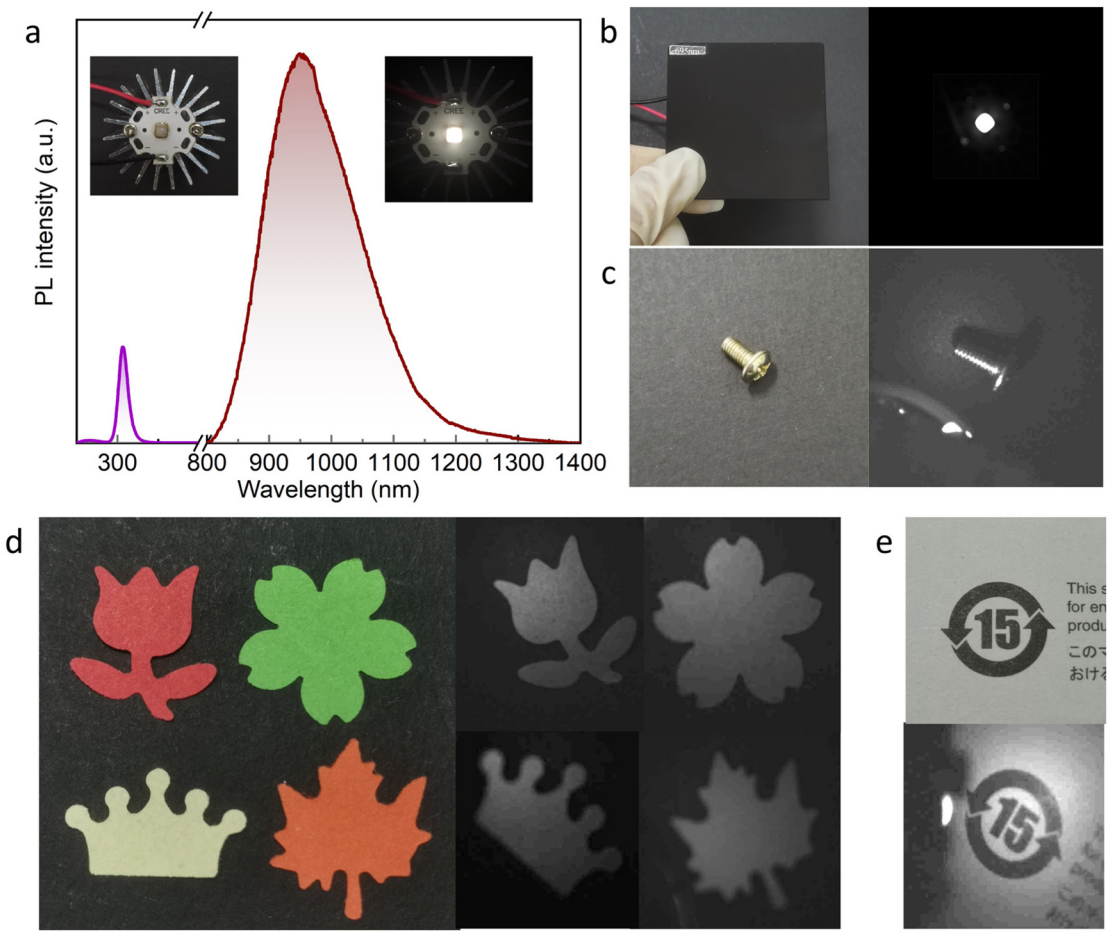


**Fig. 4** (a) Light-emitting spectrum of a NIR pc-LED device combined the as-prepared CNLC:Cr phosphor with a UV chip @ 300 nm. (b) NIR anti-counterfeiting application with a long-wavelength pass filter and (c–e) night vision imaging were recorded in daylight with a normal camera and in the dark with a NIR pc-LED camera as lighting only with a NIR camera, respectively.

 

## 4. Conclusion

In summary, we synthesized a series of $Cr^{3+}$-doped all-inorganic metal halide perovskite $Cs_2NaLuCl_6$ phosphors by a grinding and sintering method. The phosphors could be effectively excited by UV (@ 300 nm) light and demonstrated an ultra-broadband NIR emission that peaked at 960 nm and covered the NIR-I to NIR-II region of 800–1400 nm and had a FWHM of ~182 nm. It showed a very high IQE and EQE value of luminous NIR at 92.9% and 60.75%, respectively. Based on the understanding of the crystal structure, the NIR optical properties and the results of numerical simulation, we conclude that the weaker strength of the crystal field surrounding $Cr^{3+}$ is conducive to an increased odd term of the crystal field and partially release the restriction by the parity prohibition law, which improves the absorption efficiency of $Cr^{3+}$ ions. As the size of the agglomerate of the particles is close to the wavelength of NIR emission, it triggers an obvious Mie scattering effect, which is beneficial for the light extraction of radial emission from NIR luminescence. A NIR pc-LED was prepared with the $Cs_2NaLuCl_6$:$Cr^{3+}$ phosphor and a commercial UV LED chip which emitted an efficient broadband NIR, and it was demonstrated as a NIR light source for potential applications such as anti-counterfeiting and night vision imaging. The synthesis and characterization studies on $Cr^{3+}$-doped $Cs_2NaLuCl_6$ broadband NIR phosphors with very high IQE and EQE values could provide a basis for the development and applications of high-lumen broadband NIR light sources.

## Data availability

The authors confirm that the data supporting the findings of this study are available within the article [and/or its ESI†].

## Conflicts of interest

The authors declare no competing financial interest.

## Acknowledgements

This work was supported by the National Natural Science Foundation of China-Yunnan Joint Fund (U2241236), the National Natural Science Foundation of China (12204206), the Yunnan Fundamental Research Projects (202301AT070149, 202201BE070001-029), the Major Scientific and Technological Projects of Yunnan Province (202202AG050016), the International Joint Innovation Platform of Yunnan Province (202203AP140004), the Fund for Testing and Analyzing of Kunming University of Science and Technology (2022T20220051), and the Young Elite Scientists Sponsorship Program by CAST (2024QNRC001). YG acknowledges the support from the XingDian Youth Talent Plan of Yunnan Province.

## References

1 M. Vats, S. K. Mishra, M. S. Baghini, *et al.*, Near infrared fluorescence imaging in nano-therapeutics and photothermal evaluation, *Int. J. Mol. Sci.*, 2017, **18**(5), 924.
2 Y. Yang, J. Aw and B. Xing, Nanostructures for NIR light-controlled therapies, *Nanoscale*, 2017, **9**(11), 3698–3718.
3 J. T. Eells, M. T. T. Wong-Riley, J. VerHoeve, *et al.*, Mitochondrial signal transduction in accelerated wound and retinal healing by near-infrared light therapy, *Mitochondrion*, 2004, **4**(5–6), 559–567.
4 Kenry, Y. Duan and B. Liu, Recent advances of optical imaging in the second near-infrared window, *Adv. Mater.*, 2018, **30**(47), 1802394.
5 V. Rajendran, H. Chang and R. S. Liu, Recent progress on broadband near-infrared phosphors-converted light emitting diodes for future miniature spectrometers, *Opt. Mater.: X*, 2019, **1**, 100011.
6 D. Huang, H. Zhu, Z. Deng, *et al.*, A highly efficient and thermally stable broadband $Cr^{3+}$-activated double borate phosphor for near-infrared light-emitting diodes, *J. Mater. Chem. C*, 2021, **9**(1), 164–172.
7 G. N. A. De Guzman, M. H. Fang, C. H. Liang, *et al.*, Near-infrared phosphors and their full potential: A review on practical applications and future perspectives, *J. Lumin.*, 2020, **219**, 116944.
8 C. Yuan, R. Li, Y. Liu, *et al.*, Efficient and broadband $LiGaP_2O_7$: $Cr^{3+}$ phosphors for smart near-infrared light-emitting diodes, *Laser Photonics Rev.*, 2021, **15**(11), 2100227.
9 D. Hayashi, A. M. van Dongen, J. Boerekamp, *et al.*, A broadband LED source in visible to short-wave-infrared wavelengths for spectral tumor diagnostics, *Appl. Phys. Lett.*, 2017, **110**, 233701.
10 N. A. Mohd Aziz, N. Arsad, P. S. Menon, *et al.*, An assessment study of absorption effect: LED vs tungsten halogen lamp for noninvasive glucose detection, *J. Innovative Opt. Health Sci.*, 2015, **8**(02), 1550013.
11 B. Malysa, A. Meijerink, W. Wu, *et al.*, On the influence of calcium substitution to the optical properties of $Cr^{3+}$ doped $SrSc_2O_4$, *J. Lumin.*, 2017, **190**, 234–241.
12 V. Lupei, A. Lupei, C. Tiseanu, *et al.*, High-resolution optical spectroscopy of YAG: Nd: A test for structural and distribution models, *Phys. Rev. B: Condens. Matter Mater. Phys.*, 1995, **51**(1), 8.
13 J. K. Sheu, S. J. Chang, C. H. Kuo, *et al.*, White-light emission from near UV InGaN-GaN LED chip precoated with blue/green/red phosphors, *IEEE Photonics Technol. Lett.*, 2003, **15**(1), 18–20.
14 F. Zhao, H. Cai, Z. Song, *et al.*, Structural confinement for $Cr^{3+}$ activators toward efficient near-infrared phosphors with suppressed concentration quenching, *Chem. Mater.*, 2021, **33**(10), 3621–3630.
15 V. Rajendran, M. H. Fang, W. T. Huang, *et al.*, Chromium ion pair luminescence: A strategy in broadband near-infrared light-emitting diode design, *J. Am. Chem. Soc.*, 2021, **143**(45), 19058–19066.

16 Y. Xiao, W. Xiao, D. Wu, *et al.*, An extra-broadband VIS-NIR emitting phosphor toward multifunctional LED applications, *Adv. Funct. Mater.*, 2022, **32**(7), 2109618.
17 L. Zhang, D. Wang, Z. Hao, *et al.*, $Cr^{3+}$-doped broadband NIR garnet phosphor with enhanced luminescence and its application in NIR spectroscopy, *Adv. Opt. Mater.*, 2019, **7**(12), 1900185.
18 C. Liu and Y. Mei, A uniform research on the optical and EPR spectral data for the trigonal $Cr^{3+}$ center in $Cr^{3+}$-doped $Ca_3Ga_2Ge_3O_{12}$ garnet, *Optik*, 2019, **184**, 185–188.
19 Z. Pan, Y. Y. Lu and F. Liu, Sunlight-activated long-persistent luminescence in the near-infrared from $Cr^{3+}$-doped zinc gallogermanates, *Nat. Mater.*, 2012, **11**(1), 58–63.
20 Y. Wei, Z. Y. Cheng and J. Lin, An Overview on Enhancing the Stability of Lead Halide Perovskite Quantum Dots and Their Applications in Phosphor-Converted LEDs, *Chem. Soc. Rev.*, 2019, **48**, 310–350.
21 S. Ye, J. Y. Sun, Y. H. Han, Y. Y. Zhou and Q. Y. Zhang, Confining $Mn^{2+}$-Doped Lead Halide Perovskite in Zeolite-Y as Ultrastable Orange-red Phosphor Composites for White Light-Emitting Diodes, *ACS Appl. Mater. Interfaces*, 2018, **10**, 24656–24664.
22 C. L. Zhao, Y. Gao, D. C. Zhou, F. M. Zhu, J. Y. Chen and J. B. Qiu, High-Efficiency Dual-Mode Luminescence of Metal Halide Perovskite $Cs_3Bi_2Cl_9$:$Er^{3+}$ and Its Use in Optical Ttemperature Measurement with High Sensitivity, *J. Alloys Compd.*, 2023, **944**, 169134.
23 Q. Lin, Q. Wang, M. Liao, *et al.*, Trivalent chromium ions doped fluorides with both broad emission bandwidth and excellent luminescence thermal stability, *ACS Appl. Mater. Interfaces*, 2021, **13**(15), 18274–18282.
24 B. Malysa, A. Meijerink and T. Jüstel, Temperature dependent $Cr^{3+}$ photoluminescence in garnets of the type $X_3Sc_2Ga_3O_{12}$ (X = Lu, Y, Gd, La), *J. Lumin.*, 2018, **202**, 523–531.
25 A. Zabiliūtė, S. Butkutė, A. Žukauskas, *et al.*, Sol-gel synthesized far-red chromium-doped garnet phosphors for phosphor-conversion light-emitting diodes that meet the photomorphogenetic needs of plants, *Appl. Opt.*, 2014, **53**(5), 907–914.
26 Z. Jia, C. Yuan, Y. Liu, *et al.*, Strategies to approach high performance in $Cr^{3+}$-doped phosphors for high-power NIR-LED light sources, *Light: Sci. Appl.*, 2020, **9**(1), 86.
27 D. Chen, Y. Chen, H. Lu, *et al.*, A bifunctional Cr/Yb/Tm: $Ca_3Ga_2Ge_3O_{12}$ phosphor with near-infrared long-lasting phosphorescence and upconversion luminescence, *Inorg. Chem.*, 2014, **53**(16), 8638–8645.
28 J. Xiang, J. Zheng, X. Zhao, *et al.*, Synthesis of broadband NIR garnet phosphor $Ca_4ZrGe_3O_{12}$: $Cr^{3+}$, $Yb^{3+}$ for NIR pc-LED applications, *Mater. Chem. Front.*, 2022, **6**(4), 440–449.
29 N. Mao, S. Liu, Z. Song, *et al.*, A broadband near-infrared phosphor $Ca_3Y_2Ge_3O_{12}$: $Cr^{3+}$ with garnet structure, *J. Alloys Compd.*, 2021, **863**, 158699.
30 H. Xiao, J. Zhang, L. Zhang, *et al.*, $Cr^{3+}$ activated garnet phosphor with efficient blue to far-red conversion for pc-LED, *Adv. Opt. Mater.*, 2021, **9**(20), 2101134.
31 S. He, L. Zhang, H. Wu, *et al.*, Efficient super broadband NIR $Ca_2LuZr_2Al_3O_{12}$: $Cr^{3+}$, $Yb^{3+}$ garnet phosphor for pc-LED light source toward NIR spectroscopy applications, *Adv. Opt. Mater.*, 2020, **8**(6), 1901684.
32 Q. Zhang, G. Li, P. Dang, *et al.*, Enhancing and tuning broadband near-infrared (NIR) photoluminescence properties in $Cr^{3+}$-doped $Ca_2YHf_2Al_3O_{12}$ garnet phosphors via $Ce^{3+}$/$Yb^{3+}$-codoping for LED applications, *J. Mater. Chem. C*, 2021, **9**(14), 4815–4824.
33 Y. Liu, S. He, D. Wu, *et al.*, Broadband NIR garnet phosphors with improved thermal stability via energy transfer, *ACS Appl. Electron. Mater.*, 2022, **4**(2), 643–650.
34 T. Xu, L. Yuan, Y. Chen, *et al.*, $Y_3Al_5O_{12}$: $Ce^{3+}$ single crystal and red-emitting $Y_3Al_5O_{12}$: $Cr^{3+}$ single crystal for high power W-LEDs, *Opt. Mater.*, 2019, **91**, 30–34.
35 M. Mao, T. Zhou, H. Zeng, *et al.*, Broadband near-infrared (NIR) emission realized by the crystal-field engineering of $Y_{3-x}Ca_xAl_{5-x}Si_xO_{12}$: $Cr^{3+}$ (x = 0–2.0) garnet phosphors, *J. Mater. Chem. C*, 2020, **8**(6), 1981–1988.
36 L. Jiang, X. Jiang, J. Xie, *et al.*, Structural induced tunable NIR luminescence of $(Y, Lu)_3(Mg, Al)_2(Al, Si)_3O_{12}$: $Cr^{3+}$ phosphors, *J. Lumin.*, 2022, **247**, 118911.
37 X. Sun, J. Li, K. Feng, *et al.*, Luminescence characteristics of $Bi^{3+}$, $Cr^{3+}$ and $Bi^{3+}$/$Cr^{3+}$ activated $Sr_3Y_2Ge_3O_{12}$ phosphors, *J. Lumin.*, 2022, **248**, 118984.
38 H. Jiang, L. Chen, G. Zheng, *et al.*, Ultra-efficient GAGG: $Cr^{3+}$ ceramic phosphor-converted laser diode: a promising high-power compact near-infrared light source enabling clear imaging, *Adv. Opt. Mater.*, 2022, **10**(11), 2102741.
39 Y. Wang, Z. Wang, G. Wei, *et al.*, Highly efficient and stable near-infrared broadband garnet phosphor for multifunctional phosphor-converted light-emitting diodes, *Adv. Opt. Mater.*, 2022, **10**(11), 2200415.
40 E. T. Basore, W. Xiao, X. Liu, *et al.*, Broadband near-infrared garnet phosphors with near-unity internal quantum efficiency, *Adv. Opt. Mater.*, 2020, **8**(12), 2000296.
41 X. Zou, X. Wang, H. Zhang, *et al.*, A highly efficient and suitable spectral profile $Cr^{3+}$-doped garnet near-infrared emitting phosphor for regulating photomorphogenesis of plants, *Chem. Eng. J.*, 2022, **428**, 132003.
42 Y. Wang, Z. Wang, G. Wei, *et al.*, Ultra-Broadband and high efficiency Near-Infrared $Gd_3Zn_xGa_{5-2x}Ge_xO_{12}$: $Cr^{3+}$ (x = 0–2.0) garnet phosphors via crystal field engineering, *Chem. Eng. J.*, 2022, **437**, 135346.
43 W. Nie, Y. Li, J. Zuo, *et al.*, $Cr^{3+}$-activated $Na_3X_2Li_3F_{12}$ (X = Al, Ga, or In) garnet phosphors with broadband NIR emission and high luminescence efficiency for potential biomedical application, *J. Mater. Chem. C*, 2021, **9**(42), 15230–15241.
44 X. Xu, Q. Shao, L. Yao, *et al.*, Highly efficient and thermally stable $Cr^{3+}$-activated silicate phosphors for broadband near-infrared LED applications, *Chem. Eng. J.*, 2020, **383**, 123108.
45 Y. Yan, M. Shang, S. Huang, *et al.*, Photoluminescence properties of $AScSi_2O_6$: $Cr^{3+}$ (A = Na and Li) phosphors with high efficiency and thermal stability for near-infrared

 

phosphor-converted light-emitting diode light sources, *ACS Appl. Mater. Interfaces*, 2022, **14**(6), 8179–8190.

46 L. Fang, Z. Hao, L. Zhang, *et al.*, $Cr^{3+}$-doped broadband near infrared diopside phosphor for NIR pc-LED, *Mater. Res. Bull.*, 2022, **149**, 111725.

47 G. Liu, M. S. Molokeev and Z. Xia, Structural rigidity control toward $Cr^{3+}$-based broadband near-infrared luminescence with enhanced thermal stability, *Chem. Mater.*, 2022, **34**(3), 1376–1384.

48 T. Liu, H. Cai, N. Mao, *et al.*, Efficient near-infrared pyroxene phosphor $LiInGe_2O_6$: $Cr^{3+}$ for NIR spectroscopy application, *J. Am. Ceram. Soc.*, 2021, **104**(9), 4577–4584.

49 X. H. Chen, E. H. Song, Y. Y. Zhou, *et al.*, Distorted octahedral site occupation-induced high-efficiency broadband near-infrared emission in $LiScGe_2O_6$: $Cr^{3+}$ phosphor, *J. Mater. Chem. C*, 2021, **9**(39), 13640–13646.

50 W. Zhou, J. Luo, J. Fan, *et al.*, Luminescent properties and LED application of broadband near-infrared emitting $NaInGe_2O_6$: $Cr^{3+}$ phosphors, *Ceram. Int.*, 2021, **47**(18), 25343–25349.

51 X. Zhou, W. Geng, J. Li, *et al.*, An ultraviolet–visible and near-infrared-responded broadband NIR phosphor and its NIR spectroscopy application, *Adv. Opt. Mater.*, 2020, **8**(8), 1902003.

52 H. Liu, F. Zhao, H. Cai, *et al.*, Consequence of optimal bonding on cation ordering and enhanced near-infrared luminescence in $Cr^{3+}$-doped pyroxene oxides, *J. Mater. Chem. C*, 2022, **10**(24), 9232–9240.

53 L. Yao, Q. Shao, S. Han, *et al.*, Enhancing near-infrared photoluminescence intensity and spectral properties in $Yb^{3+}$ codoped $LiScP_2O_7$: $Cr^{3+}$, *Chem. Mater.*, 2020, **32**(6), 2430–2439.

54 H. Zhang, J. Zhong, X. Zhang, *et al.*, Achieving an ultra-broadband infrared emission through efficient energy transfer in $LiInP_2O_7$: $Cr^{3+}$, $Yb^{3+}$ phosphor, *J. Alloys Compd.*, 2022, **894**, 162386.

55 L. Zeng, J. Zhong, C. Li, *et al.*, Broadband near-infrared emission in the $NaInP_2O_7$: $Cr^{3+}$ phosphor for light-emitting-diode applications, *J. Lumin.*, 2022, **247**, 118909.

56 H. Zhang, J. Zhong, F. Du, *et al.*, Efficient and thermally stable broad-band near-infrared emission in a $KAlP_2O_7$: $Cr^{3+}$ phosphor for nondestructive examination, *ACS Appl. Mater. Interfaces*, 2022, **14**(9), 11663–11671.

57 F. Y. Zhao, H. Cai, S. Y. Zhang, *et al.*, Octahedron-dependent near-infrared luminescence in $Cr^{3+}$-activated phosphors, *Mater. Today Chem.*, 2022, **23**, 100704.

58 Q. Shao, H. Ding, L. Yao, *et al.*, Photoluminescence properties of a $ScBO_3$: $Cr^{3+}$ phosphor and its applications for broadband near-infrared LEDs, *RSC Adv.*, 2018, **8**(22), 12035–12042.

59 Z. Sun, Q. Ning, W. Zhou, *et al.*, Structural and spectroscopic investigation of an efficient and broadband NIR phosphor $InBO_3$: $Cr^{3+}$ and its application in NIR pc-LEDs, *Ceram. Int.*, 2021, **47**(10), 13598–13603.

60 Y. Zhang, S. Miao, Y. Liang, *et al.*, Blue LED-pumped intense short-wave infrared luminescence based on $Cr^{3+}$-$Yb^{3+}$-co-doped phosphors, *Light: Sci. Appl.*, 2022, **11**(1), 136.

61 T. Gao, W. Zhuang, R. Liu, *et al.*, Design of a broadband NIR phosphor for security-monitoring LEDs: tunable photoluminescence properties and enhanced thermal stability, *Cryst. Growth Des.*, 2020, **20**(6), 3851–3860.

62 H. Wu, L. Jiang, K. Li, *et al.*, Design of broadband near-infrared $Y_{0.57}La_{0.72}Sc_{2.71}(BO_3)_4$: $Cr^{3+}$ phosphors based on one-site occupation and their application in NIR light-emitting diodes, *J. Mater. Chem. C*, 2021, **9**(35), 11761–11771.

63 T. Gao, W. Zhuang, R. Liu, *et al.*, Design and control of the luminescence in $Cr^{3+}$-doped NIR phosphors via crystal field engineering, *J. Alloys Compd.*, 2020, **848**, 156557.

64 D. Wu, L. Liu, H. Liang, *et al.*, $LiBAlF_6$: $Cr^{3+}$ (B = Ca, Sr) fluoride phosphors with ultra-broad near-infrared emission for NIR pc-LEDs, *Ceram. Int.*, 2022, **48**(1), 387–396.

65 Y. Zhang, Y. Liang, S. Miao, *et al.*, Broadband near-infrared $BaMSi_3O_9$: $Cr^{3+}$ (M = Zr, Sn, Hf) phosphors for light-emitting diode applications, *Inorg. Chem. Front.*, 2021, **8**(24), 5186–5194.

66 S. Ding, H. Guo, P. Feng, *et al.*, A new near-infrared long persistent luminescence material with its outstanding persistent luminescence performance and promising multifunctional application prospects, *Adv. Opt. Mater.*, 2020, **8**(18), 2000097.

67 J. Qiu, Q. Wang, D. Zhou, *et al.*, Disentangling site occupancy, cation regulation, and oxidation state regulation of the broadband near infrared emission in a chromium-doped $SrGa_4O_7$ phosphor, *Inorg. Chem. Front.*, 2020, **7**(12), 2313–2321.

68 L. Ao, Y. Tang, J. Li, *et al.*, Structure characterization and microwave dielectric properties of $LiGa_5O_8$ ceramic with low-$\varepsilon_r$ and low loss, *J. Eur. Ceram. Soc.*, 2020, **40**(15), 5498–5503.

69 L. Kong, Y. Liu, L. Dong, *et al.*, Near-infrared emission of $CaAl_6Ga_6O_{19}$: $Cr^{3+}$, $Ln^{3+}$ (Ln = Yb, Nd, and Er) via energy transfer for c-Si solar cells, *Dalton Trans.*, 2020, **49**(25), 8791–8798.

70 Y. Han, L. Shi, H. Liu, *et al.*, A novel far red-emitting phosphor $SrMgAl_{10}O_{17}$: $Cr^{3+}$ for warm w-LEDs, *Optik*, 2019, **195**, 162014.

71 L. You, R. Tian, T. Zhou, *et al.*, Broadband near-infrared phosphor $BaMgAl_{10}O_{17}$: $Cr^{3+}$ realized by crystallographic site engineering, *Chem. Eng. J.*, 2021, **417**, 129224.

72 L. Yao, Q. Shao, M. Shi, *et al.*, Efficient ultra-broadband $Ga_4GeO_8$: $Cr^{3+}$ phosphors with tunable peak wavelengths from 835 to 980 nm for NIR pc-LED application, *Adv. Opt. Mater.*, 2022, **10**(4), 2102229.

73 Q. Bai, S. Zhao, L. Guan, *et al.*, Design and control of the luminescence of $Cr^{3+}$-doped phosphors in the near-infrared I region by fitting the crystal field, *Cryst. Growth Des.*, 2018, **18**(5), 3178–3186.

74 D. Huang, X. He, J. Zhang, *et al.*, Efficient and thermally stable broadband near-infrared emission from near zero thermal expansion $AlP_3O_9$: $Cr^{3+}$ phosphors, *Inorg. Chem. Front.*, 2022, **9**(8), 1692–1700.

75 T. Yu, H. Sheng, S. Chen, *et al.*, A broadband near-infrared $Sc_{1-x}(PO_3)_3$: $XCr^{3+}$ phosphor with enhanced thermal stability and quantum yield by $Yb^{3+}$ codoping, *J. Am. Ceram. Soc.*, 2022, **105**(5), 3403–3417.
76 C. Zhong, L. Zhang, Y. Xu, *et al.*, Novel broadband near-infrared emitting phosphor $LiGe_2(PO_4)_3$: $Cr^{3+}$ with tuning and enhancement of NIR emission by codoping $Sb^{5+}$, *J. Alloys Compd.*, 2022, **903**, 163945.
77 X. Zhang, L. Zhang, Y. Xu, *et al.*, Broadband near-infrared-emitting phosphors with suppressed concentration quenching in a two-dimensional structure, *Inorg. Chem.*, 2022, **61**(19), 7597–7607.
78 S. Miao, Y. Liang, Y. Zhang, *et al.*, Spectrally tunable and thermally stable near-infrared luminescence in $Na_3Sc_2(PO_4)_3$: $Cr^{3+}$ phosphors by $Ga^{3+}$ co-doping for light-emitting diodes, *J. Mater. Chem. C*, 2022, **10**(3), 994–1002.
79 J. Wang, L. Jiang, R. Pang, *et al.*, $Cr^{3+}$-doped borate phosphors for broadband near-infrared LED applications, *Inorg. Chem. Front.*, 2022, **9**(10), 2240–2251.
80 J. Lin, L. Zhou, L. Ren, *et al.*, Broadband near-infrared emitting $Sr_3Sc_4O_9$: $Cr^{3+}$ phosphors: Luminescence properties and application in light-emitting diodes, *J. Alloys Compd.*, 2022, **908**, 164582.
81 J. Lai, W. Shen, J. Qiu, *et al.*, Broadband near-infrared emission enhancement in $K_2Ga_2Sn_6O_{16}$: $Cr^{3+}$ phosphor by electron-lattice coupling regulation, *J. Am. Ceram. Soc.*, 2020, **103**(9), 5067–5075.
82 G. Liu, T. Hu, M. S. Molokeev, *et al.*, Li/Na substitution and $Yb^{3+}$ co-doping enabling tunable near-infrared emission in $LiIn_2SbO_6$: $Cr^{3+}$ phosphors for light-emitting diodes, *iScience*, 2021, **24**, 102250.
83 Q. Zhang, D. Liu, P. Dang, *et al.*, Two selective sites control of $Cr^{3+}$-doped $ABO_4$ phosphors for tuning ultra-broadband near-infrared photoluminescence and multi-applications, *Laser Photonics Rev.*, 2022, **16**(2), 2100459.
84 L. Lou, S. Zhao, S. Yuan, *et al.*, Efficient broadband near-infrared emission induced by $Nb^{5+}$ substitution for $Ta^{5+}$ in $GaTa_{1-y}Nb_yO_4$: $Cr^{3+}$ phosphor, *Inorg. Chem. Front.*, 2022, **9**(14), 3522–3531.
85 X. Zhou, J. Xiang, J. Zheng, *et al.*, Ab initio two-sites occupancy and broadband near-infrared emission of $Cr^{3+}$ in $Li_2MgZrO_4$, *Mater. Chem. Front.*, 2021, **5**(11), 4334–4342.
86 T. Tan, S. Wang, J. Su, *et al.*, Design of a novel near-infrared luminescence material $Li_2Mg_3TiO_6$: $Cr^{3+}$ with an ultra-wide tuning range applied to near-infrared light-emitting diodes, *ACS Sustainable Chem. Eng.*, 2022, **10**(12), 3839–3850.
87 S. Zhang, Y. Liu, J. Yin, *et al.*, A novel $Cr^{3+}$-activated far-red titanate phosphor: synthesis, luminescence enhancement and application prospect, *Mater. Today Chem.*, 2022, **24**, 100835.
88 J. Zhou, Z. Long, J. Qiu, *et al.*, Broadband near-infrared emitting from $Li_{1.6}Zn_{1.6}Sn_{2.8}O_8$:$Cr^{3+}$ phosphor by two-site occupation and $Al^{3+}$ cationic regulation, *Mater. Des.*, 2020, **192**, 108701.
89 Z. H. Zheng, B. M. Liu, Z. Zhou, *et al.*, A simple and generic post-treatment strategy for highly efficient $Cr^{3+}$-activated broadband NIR emitting phosphors for high-power NIR light sources, *J. Mater. Chem. C*, 2022, **10**(22), 8797–8805.
90 F. Zhu, Y. Gao, C. Zhao, *et al.*, Achieving Broadband NIR-I to NIR-II Emission in an All-Inorganic Halide Double-Perovskite $Cs_2NaYCl_6$: $Cr^{3+}$ Phosphor for Night Vision Imaging. ACS Applied Materials & Interfaces, *ACS Appl. Mater. Interfaces*, 2023, **15**(33), 39550–39558.
91 R. Valiente, F. Rodríguez, J. González, *et al.*, High pressure optical spectroscopy of $Ce^{3+}$-doped $Cs_2NaLuCl_6$, *Chem. Phys. Lett.*, 2009, **481**(1–3), 149–151.
92 C. Chen, M. Jin, J. Xiang, *et al.*, Blue-red dual color emitting phosphor $Cs_2NaLuCl_6$: $Sb^{3+}$, $Ho^{3+}$ for plant growth LEDs, *Ceram. Int.*, 2023, **49**(15), 25232–25239.
93 G. C. Allen and P. M. Tucker, Multiplet splitting of X-ray photoelectron lines of chromium complexes. The effect of covalency on the 2p core level spin-orbit separation, *Inorg. Chim. Acta*, 1976, **16**, 41–45.
94 M. Vrankić, B. Gržeta, D. Lützenkirchen-Hecht, *et al.*, Chromium environment within Cr-doped $BaAl_2O_4$: correlation of X-ray diffraction and X-ray absorption spectroscopy investigations, *Inorg. Chem.*, 2015, **54**(23), 11127–11135.
95 V. Singh, G. Sivaramaiah, J. L. Rao, *et al.*, EPR and optical investigations of $LaMgAl_{11}O_{19}$: $Cr^{3+}$ phosphor, *Mater. Res. Bull.*, 2014, **60**, 397–400.
96 Q. Ke-Yuan, M. Jun, F. Wei, *et al.*, Research on scattering properties of phosphor for high power white light emitting diode based on Mie scattering theory, *Acta Phys. Sin.*, 2012, **61**, 204201.
97 Y. Gao, L. Liu, S. Murai, *et al.*, Enhancing up-conversion luminescence using dielectric metasurfaces: role of the quality factor of resonance at a pumping wavelength, *ACS Appl. Mater. Interfaces*, 2023, **15**(39), 45960–45969.
98 Y. Gao, S. Murai, K. Shinozaki, *et al.*, Aluminum for near infrared plasmonics: amplified up-conversion photoluminescence from core-shell nanoparticles on periodic lattices, *Adv. Opt. Mater.*, 2021, **9**(1), 2001040.
99 Y. Gao, S. Murai, K. Shinozaki, *et al.*, Up-conversion luminescence enhanced by the plasmonic lattice resonating at the transparent window of water, *ACS Appl. Energy Mater.*, 2021, **4**(4), 2999–3007.
100 X. Lu, Y. Gao, J. Chen, *et al.*, Long-Wavelength Near-Infrared Divalent Nickel-Activated Double-Perovskite $Ba_2MgWO_6$ Phosphor as Imaging for Human Fingers, *ACS Appl. Mater. Interfaces*, 2023, **15**(33), 39472–39479.
101 F. Zhu, Y. Gao, J. Ding, *et al.*, Synergistic enhancement of the near-infrared luminescence properties of $Ni^{2+}$-doped $SrTiO_3$ perovskite phosphors and their application, *J. Mater. Chem. C*, 2023, **11**(30), 10236–10246.
102 F. Zhu, Y. Gao, J. Ding, *et al.*, An efficient strategy of charge compensation for $Ni^{2+}$-activated $SrTiO_3$ perovskite near-infrared phosphor toward optical imaging illumination, *Ceram. Int.*, 2023, **49**(18), 30613–30622.

 

103 J. Ren, F. Zhu, Y. Gao, *et al.*, Ultra-broadband Near-infrared emission of $Cr^{3+}$-containing Oxy-fluoride Glass-ceramics, *Ceram. Int.*, 2024, **50**(17), 31474–31481.
104 M. Tan, Y. Gao, J. Chen, *et al.*, A Nickel-doped, lanthanum gallium germanate-based phosphor as an ultra-broadband short-wavelength infrared region emitter for optical imaging, *Ceram. Int.*, 2024, **50**(13), 23685–23693.
105 Y. Deng, F. Zhu, Y. Gao, *et al.*, Strategy of Charge Compensation for High-Performance $Ni^{2+}$-Activated $MgAl_2O_4$ Spinel Near-Infrared Phosphor Synthesis via the Sol-Gel Combustion Method, *Inorg. Chem.*, 2024, **63**(14), 6555–6563.
106 Y. Deng, Y. Gao, F. Zhu, *et al.*, Sol-gel combustion synthesis and near-infrared luminescence of $Ni^{2+}$-doped $MgAl_2O_4$ spinel phosphor, *Ceram. Int.*, 2024, **50**(7), 12319–12325.
107 W. H. Baur, The geometry of polyhedral distortions. Predictive relationships for the phosphate group, *Acta Crystallogr., Sect. B: Struct. Crystallogr. Cryst. Chem.*, 1974, **30**(5), 1195–1215.
108 S. Liao, X. Ji, Y. Liu, *et al.*, Highly efficient and thermally stable blue-green $(Ba_{0.8}Eu_{0.2}O)(Al_2O_3)_{4.575\times(1+x)}$ phosphor through structural modification, *ACS Appl. Mater. Interfaces*, 2018, **10**(45), 39064–39073.
109 X. Ji, J. Zhang, Y. Li, *et al.*, Improving quantum efficiency and thermal stability in blue-emitting $Ba_{2-x}Sr_xSiO_4$: $Ce^{3+}$ phosphor via solid solution, *Chem. Mater.*, 2018, **30**(15), 5137–5147.
110 Y. Xiao, Z. Hao, L. Zhang, *et al.*, An efficient blue phosphor $Ba_2Lu_5B_5O_{17}$: $Ce^{3+}$ stabilized by $La_2O_3$: Photoluminescence properties and potential use in white LEDs, *Dyes Pigm.*, 2018, **154**, 121–127.
111 E. Song, Y. Zhou, X. B. Yang, *et al.*, Highly efficient and stable narrow-band red phosphor $Cs_2SiF_6$: $Mn^{4+}$ for high-power warm white LED applications, *ACS Photonics*, 2017, **4**(10), 2556–2565.
112 J. Qiao, S. Zhang, X. Zhou, *et al.*, Near-Infrared Light-Emitting Diodes utilizing a Europium-Activated Calcium Oxide Phosphor with External Quantum Efficiency of up to 54.7%, *Adv. Mater.*, 2022, **34**(26), 2201887.
113 Y. Gao, S. Murai, F. Zhang, *et al.*, Enhancing upconversion photoluminescence by plasmonic-photonic hybrid mode, *Opt. Express*, 2020, **28**(2), 886–897.
114 Y. Gao, S. Murai, K. Shinozaki, *et al.*, Up-to-Five-Photon Upconversion from Near-Infrared to Ultraviolet Luminescence Coupled to Aluminum Plasmonic Lattices, *ACS Appl. Mater. Interfaces*, 2023, **15**(7), 9533–9541.
115 J. Ren, F. Zhu, Y. Gao, *et al.*, Ultra-broadband Near-infrared emission of $Cr^{3+}$-containing Oxy-fluoride Glass-ceramics, *Ceram. Int.*, 2024, **50**(17), 31474–31481.
116 M. Tan, Y. Gao, J. Chen, *et al.*, A Nickel-doped, lanthanum gallium germanate-based phosphor as an ultra-broadband short-wavelength infrared region emitter for optical imaging, *Ceram. Int.*, 2024, **50**(13), 23685–23693.
117 Y. Deng, F. Zhu, Y. Gao, *et al.*, Strategy of Charge Compensation for High-Performance $Ni^{2+}$-Activated $MgAl_2O_4$ Spinel Near-Infrared Phosphor Synthesis via the Sol-Gel Combustion Method, *Inorg. Chem.*, 2024, **63**(14), 6555–6563.
118 Y. Deng, Y. Gao, F. Zhu, *et al.*, Sol-gel combustion synthesis and near-infrared luminescence of $Ni^{2+}$-doped $MgAl_2O_4$ spinel phosphor, *Ceram. Int.*, 2024, **50**(7), 12319–12325.
119 C. Zhao, Y. Gao, J. Wang, *et al.*, Achieving nearly quantitative (~100%) IQE and 42.3% EQE across NIR-I and NIR-II regions with $Cr^{3+}$-doped $Cs_2NaScCl_6$ under 300 nm excitation, *Laser Photonics Rev.*, 2024, **18**(3), 2300952.
120 J. Chen, Y. Gao, M. Tan, *et al.*, Cation substitution-dependent phase transforming phosphors: A new alternative broadband NIR-II emitter for solid state lighting, *J. Alloys Compd.*, 2023, **965**, 171311.
121 Y. Gao, B. Wang, L. Liu, *et al.*, Near-infrared engineering for broad-band wavelength-tunable in biological window of NIR-II and-III: A solid solution phosphor of $Sr_{1-x}Ca_xTiO_3$: $Ni^{2+}$, *J. Lumin.*, 2021, **238**, 118235.
122 Y. Gao, B. Wang, L. Liu, *et al.*, Near-infrared engineering for broad-band wavelength-tunable in biological window of NIR-II and-III: A solid solution phosphor of $Sr_{1-x}Ca_xTiO_3$: $Ni^{2+}$, *J. Lumin.*, 2021, **238**, 118235.
123 Y. Gao, J. Qiu and D. Zhou, Investigation of optical properties: Eu with Al codoping in aluminum silicate glasses and glass-ceramics, *J. Am. Ceram. Soc.*, 2017, **100**(7), 2901–2913.
124 J. Chen, Y. Gao, J. Chen, *et al.*, Designing and controlling the $Ni^{2+}$-activated (Zn, Mg)$Al_2O_4$ spinel solid-solution for phosphor-converted broadband near-infrared illumination, *J. Mater. Chem. C*, 2023, **11**(6), 2217–2228.
125 F. Zhu, Y. Gao, B. Zhu, *et al.*, $Ni^{2+}$-doped $MgTa_2O_6$ phosphors capable of near-infrared II and III emission under blue-light excitation, *Chem. Eng. J.*, 2024, **479**, 147568.
126 C. Zhao, Y. Gao and J. Qiu, Achieving multicolor emitting of antimony-doped indium-based halide perovskite via monovalent metal induced phase engineering, *ACS Appl. Mater. Interfaces*, 2023, **15**(51), 59610–59617.